

RESONANT DEGENERATE FOUR-WAVE MIXING IN A RUBY CRYSTAL

LUÍS M. BERNARDO

Laboratório de Física, Faculdade de Ciências, Universidade do Porto, 4000 Porto, Portugal

(Received 30 November 1984)

ABSTRACT—We study degenerate four-wave mixing (DFWM) in a ruby crystal, theoretically and experimentally, in isotropic and anisotropic configurations. We show that thermal DFWM is negligible when compared with resonant DFWM and this one is not affected by self-focusing. Finally we present phase conjugate reconstruction of a microscopic object as an application of DFWM.

1 — FOUR-WAVE MIXING (FWM)

FWM refers to the interaction of four waves in a non-linear medium. The term "Degenerate Four-Wave Mixing" (DFWM) is used when the waves have all the same frequency. The geometrical configuration for the interaction, where two counter-propagating pump waves are used with a probe beam at some angle ϕ , is sometimes called "backward DFWM" interaction (see Fig. 1). In

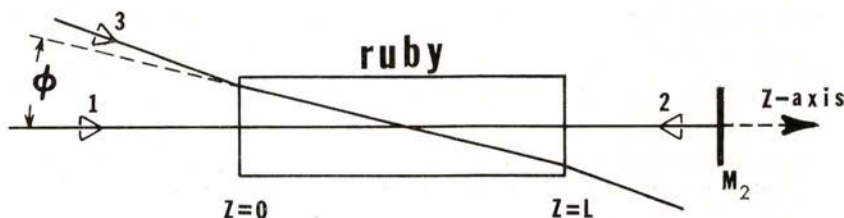


Fig. 1 — Relative positions of the pump beams 1, 2 and the probe beam 3. The angle ϕ is the angle between 1 and 3, inside the crystal. The z-axis has the same direction as beam 1. M_2 is the mirror where beam 1 is reflected to generate beam 2.

this way, the process can be distinguished from the forward DFWM [1], where only one pump with a probe generate a forward phase conjugate signal. This interaction corresponds to 3-wave mixing; but, as the pump acts as if it is formed by two forward pumps (or equivalently, two pump photons take part in the reaction), it can be considered a FWM process. We use "DFWM" instead of "backward DFWM" for simplicity during the exposition, since this is the only configuration we consider in this paper.

The non-linear nature of DFWM implies that the response of the optical medium to the light fields is not linear, i.e. the polarization $\mathbf{P}(\mathbf{r}, t)$ of the medium has terms which are non-linear functions of the electric field $\mathbf{E}(\mathbf{r}, t)$. Because four waves are involved, the first important term of the non-linear polarization, when expanded in powers of $\mathbf{E}(\mathbf{r}, t)$, is of third order [2]

$$\mathbf{P}^{\text{NL}}(\mathbf{r}, t) = \chi^{(3)} : \mathbf{E} \mathbf{E} \mathbf{E} \quad (1)$$

where $\chi^{(3)}$ is the third order tensor susceptibility and

$$\mathbf{E} = \sum_j \mathbf{E}_j(\omega) \quad (j = 1, 2, 3, 4) \quad (2)$$

is the field.

For isotropic media and when only the polarization of frequency ω is considered, the condensed expression (1) reduces [3] to

$$\mathbf{P}^{\text{NL}} = \alpha (\mathbf{E} \cdot \mathbf{E}^*) \mathbf{E} + \gamma (\mathbf{E} \cdot \mathbf{E}) \mathbf{E}^* \quad (3)$$

The first term leads to the holographic analogy [4, 5], where each pump acts as the reading beam, generating the phase conjugate beam. The second term describes the oscillation at frequency 2ω of the non-linear index of refraction which scatters one of the waves to generate the fourth [6] (parametric interaction). The coefficients α and γ can be made large by choosing the right non-linear medium: one-photon resonant medium for large α , two-photon resonant medium for large γ . Ruby behaves like a one-photon resonant medium and therefore a larger α is expected.

If multi-photon processes are important, odd terms of the polarization higher than the third power of \mathbf{E} have to be considered, since their coefficients cannot be neglected.

The above considerations and general expressions for \mathbf{P}^{NL} are valid for any non-linear medium. The expressions for the

susceptibility χ and for the parameters α and γ , however, result from the particular non-linear mechanism involved. In our medium, ruby, the mechanism is resonant absorption and the expressions that will be obtained are valid in general for those media. Therefore, although the theory in this paper refers specifically to a ruby crystal, it can be applied to any resonant absorber, after evaluating the corrections caused by different valued parameters.

2 — RUBY CRYSTAL DESCRIPTION

A ruby crystal is a crystal of sapphire (Al_2O_3) where a certain percentage of Al^{3+} ions has been replaced by chromium ions Cr^{3+} , which cause the pink color of the otherwise colorless sapphire crystal. The Cr_2O_3 doping percentage in our crystal is 0.05 wt.%, i. e. the concentration of Cr^{3+} ions is 1.58×10^{19} ions. cm^{-3} .

In the free Cr atom ($Z = 24$), the shells from 1s through 3p are completely filled; shell 3d has five electrons ($3d^5$) and shell 4s has one electron ($4s^1$). When the Cr atoms are introduced into the host crystal of sapphire, they share, in the bonding, three electrons with O^{2-} , becoming Cr^{3+} . One of those electrons comes from the 4s shell and the other two from the 3d shell. The 3d shell, which can be occupied with 10 electrons, is then only partially filled with two electrons. The possible arrangements of these two electrons in the 3d shell leads to the energy levels of the Cr^{3+} ions in the Al_2O_3 host crystal [7]. When those ions form a solid like the ruby crystal, the energy levels for the crystal will be much more complicated than the ones for an isolated Cr^{3+} ion.

In Fig. 2 we show a detailed energy level diagram of ruby [8] that has been obtained experimentally. For the optical frequency we used (the blue/green light of the Ar laser), the diagram of Fig. 2 can be simplified for that of Fig. 3. The Ar laser light excites the ions from ground state 1 to the excited level 3. From level 3 they decay non radiatively and very fast (< 1 ns) [9] to level 2. The decay time from level 2 to level 1 is comparatively slow, $\tau \approx 3$ ms at 300 K and 4.3 ms at 77 K [10]. Absorption coefficients for ruby when it is in the excited level 2 have been measured [11]. Those results show that transitions from level 2 to

higher levels (dashed lines in Fig. 2) may take place. However the effect of the excited states' absorption is usually small [9]. Nevertheless, we will consider its effect in the latter calculations of the induced polarization.

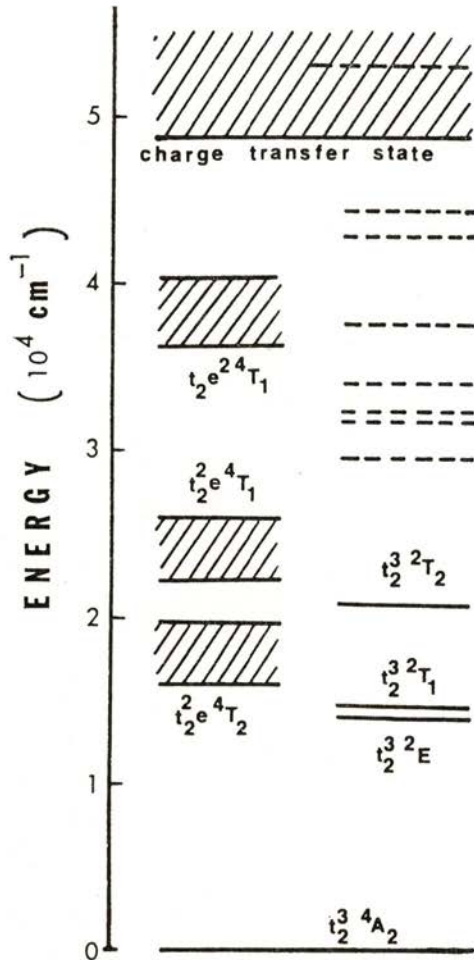


Fig. 2 — Energy level diagram of ruby [8].

The ruby crystal geometry is shown in Fig. 4. Its nonpolished 5×11 mm² surfaces make a 60° angle with the c-axis. Both pairs

of polished surfaces $5 \times 11 \text{ mm}^2$ and $5 \times 5 \text{ mm}^2$ can be used for the entrance of the beams.

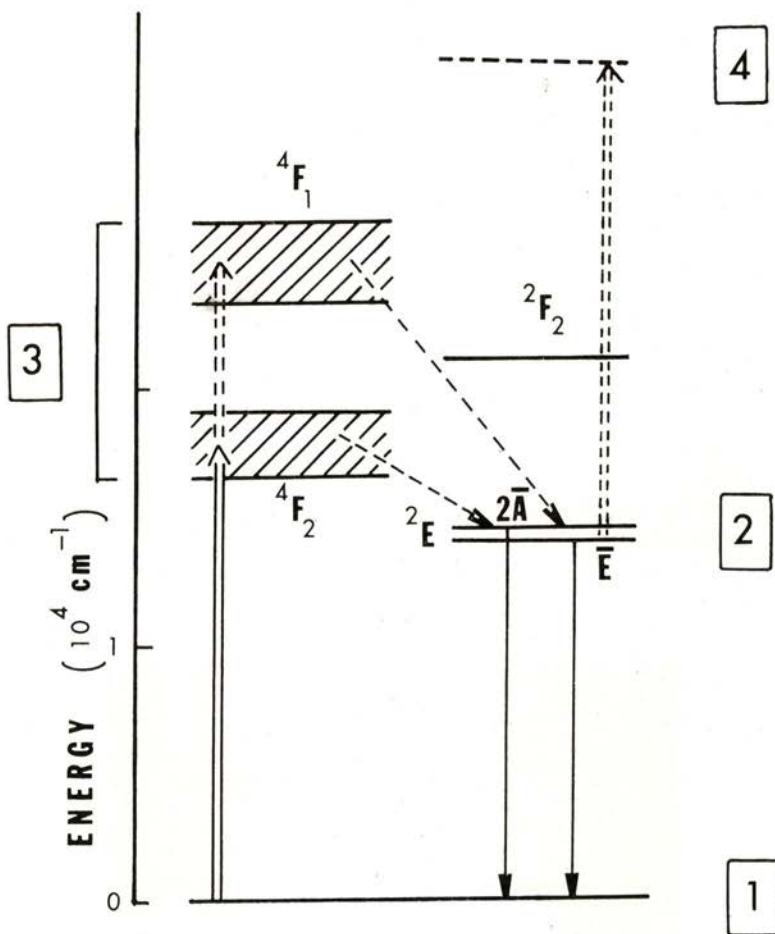


Fig. 3—Energy level diagram of ruby used for calculations on induced polarization.

The position of the c-axis has been determined by analysis of bi-refringence patterns caused by a convergent beam, incident on the crystal and observed through a polarizer [12]. Figs. 5 and 6 show those patterns for two different orientations of the crystal.

Fig. 5 refers to the transversal orientation, where the laser beam is incident on $5 \times 11 \text{ mm}^2$ polished surfaces. Fig. 6 refers to the

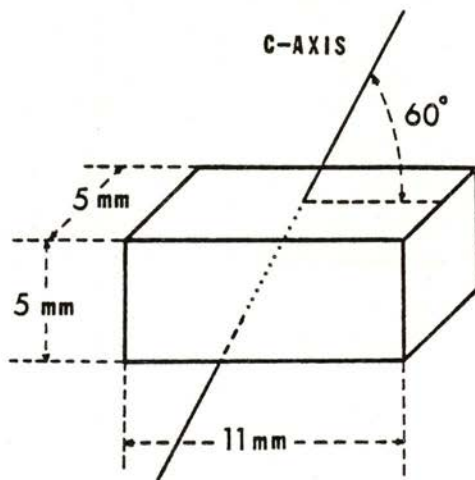


Fig. 4 — Ruby crystal geometry. The c-axis makes a 60° angle with the non-polished surface $5 \times 11 \text{ mm}^2$ and it is parallel to the polished surfaces $5 \times 11 \text{ mm}^2$.

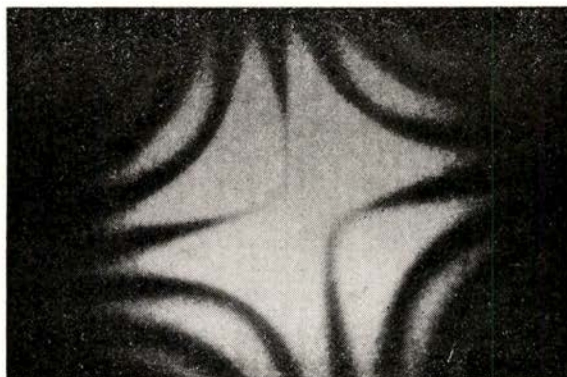


Fig. 5 — Birefringence pattern for the transversal orientation of the crystal.

longitudinal orientation where the beam is incident on the $5 \times 5 \text{ mm}^2$ polished faces of the crystal.

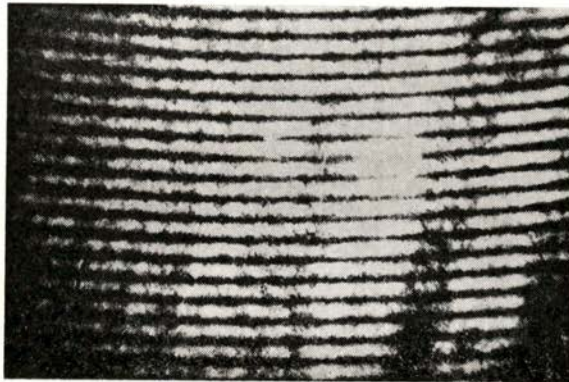


Fig. 6 — Birefringence pattern for the longitudinal orientation of the crystal.

3 — SEMICLASSICAL THEORY OF RESONANT DFWM

In this paper we study the case where the system in Fig. 3 can be decomposed in two independent subsystems 1, 2, 3 and 2, 4; the transition $3 \rightarrow 2$ is nonradiative and the exciting field is in resonance only with the transitions $1 \rightarrow 3$ and $2 \rightarrow 4$.

This approach implies that pumping from level 2 to level 4 is negligible for the calculations carried on the subsystem 1, 2, 3. In other words, the absorption from the excited level 2 is small enough not to change significantly the population of level 2.

We study first the subsystem 1, 2, 3 and then the subsystem 2, 4 as a particular case of it. Finally we get the expressions for the whole system.

We use the semiclassical theory of interaction in the electric dipole approximation [13], with the Hermitian density operator ρ [14]. After neglecting thermal excitation, the equations of motion (Bloch equations) for the density matrix elements ρ_{ij} can be written, introducing relaxation terms [15] as

$$\dot{\rho}_{11} = - (i/\hbar) (V_{13} \rho_{31} - \rho_{13} V_{31}) + \rho_{22} / \tau_{21} + \rho_{33} / \tau_{31} \quad (4a)$$

$$\dot{\rho}_{22} = - \rho_{22} / \tau_{21} + \rho_{33} / \tau_{32} \quad (4b)$$

$$\dot{\rho}_{33} = - (i/\hbar) (V_{31} \rho_{13} - \rho_{31} V_{13}) - \rho_{33} (1/\tau_{31} + 1/\tau_{32}) \quad (4c)$$

$$\dot{\rho}_{13} = - i \omega_{13} \rho_{13} - (i/\hbar) V_{13} (\rho_{33} - \rho_{11}) - \rho_{13} / T \quad (4d)$$

where V_{ij} is the matrix element of the energy of interaction

$V = -\mu \cdot \mathbf{E}$ with μ as the electric dipole operator and $\mathbf{E} = \sum_m (\mathbf{A}_m / 2) \exp [i(\omega t - \mathbf{k}_m \cdot \mathbf{r})] + \text{c.c.}$ is the exciting electric field; τ_{ij} is the lifetime of the excited level i before decaying to level j ; T is the transverse relaxation time and ω_{ij} is the frequency associated to the energy difference of levels i and j .

From eq. (4d) it is seen that nondriven ($\mathbf{E} = 0$) behaviour of ρ_{13} is given by

$$\rho_{13} = \rho_{13}(0) \exp [-(i\omega_{13} + 1/T)t] = \lambda_{13}(t) \exp(i\omega_{31}t) \quad (5)$$

where $\lambda_{13}(t) = \rho_{13}(0) \exp(-t/T)$ is a time varying slow function, $T^{-1} \ll \omega_{31} = -\omega_{13}$ [16].

When terms in $\exp(\pm 2i\omega t)$ are ignored and after using the probability conservation equation, we can write eq. 4, in the steady state regime, as:

$$\rho_{11} + \rho_{22} + \rho_{33} = 1 \quad (6a)$$

$$\rho_{22} = (\tau_{21} / \tau_{32}) \rho_{33} \quad (6b)$$

$$\begin{aligned} \hbar^{-1} (1 + \delta^2)^{-1} |\mu_{13}|^2 (\rho_{11} - \rho_{33}) \sum_{lm} 1/2 \mathbf{A}_l \cdot \mathbf{A}_m^* \\ \exp [-i(\mathbf{k}_l - \mathbf{k}_m) \cdot \mathbf{r}] - \rho_{33} (\tau_{31}^{-1} + \tau_{32}^{-1}) = 0 \end{aligned} \quad (6c)$$

$$\lambda_{13} = -(i + \delta) (i + \delta^2)^{-1} \mu_{13} (\rho_{11} - \rho_{33}) \sum_m 1/2 \mathbf{A}_m \exp(-i\mathbf{k}_m \cdot \mathbf{r}) \quad (6d)$$

where $\delta \equiv (\omega - \omega_{31}) T$ is the normalized detuning of the field from the line center. The solutions of eq 6 are:

$$\rho_{11} = (1 + \alpha I / I_{\text{SAT}}) / (1 + \beta I / I_{\text{SAT}}) \quad (7a)$$

$$\rho_{22} = (I / I_{\text{SAT}}) / (1 + \beta I / I_{\text{SAT}}) \quad (7b)$$

$$\rho_{33} = (\alpha I / I_{\text{SAT}}) / (1 + \beta I / I_{\text{SAT}}) \quad (7c)$$

$$\begin{aligned} \rho_{13} = -\mu_{13} T \hbar^{-1} (i + \delta) (1 + \delta^2)^{-1} (1 + \beta I / I_{\text{SAT}})^{-1} \\ \sum_m 1/2 \mathbf{A}_m \exp [i(\omega t - \mathbf{k}_m \cdot \mathbf{r})] \end{aligned} \quad (7d)$$

where $\alpha = \tau_{32} / \tau_{21}$, $\beta = 2\alpha + 1$, $Q = (1 + \tau_{32} / \tau_{31})^{-1}$

$$I_{\text{SAT}} = \hbar^2 (1 + \delta^2) / (|\mu_{13}|^2 T \tau_{21} Q),$$

$$I = 1/2 \sum_{l,m} \mathbf{A}_l \cdot \mathbf{A}_m^* e^{-i(\mathbf{k}_l - \mathbf{k}_m) \cdot \mathbf{r}} + \text{c.c.}$$

The magnitude of the induced real polarization is

$$P = N \langle \mu \rangle = N (\mu_{31} \rho_{13} + \mu_{13} \rho_{31}) \quad (8)$$

where N is the number density of the absorption centers (Cr^{3+} ions). The real polarization associated with the subsystem 1, 2, 3 is then:

$$P = - \frac{\epsilon_0 \alpha_0}{k (1 + \delta^2)} \frac{\sum_m \mathbf{A}_m [\delta \cos(\omega t - \mathbf{k}_m \cdot \mathbf{r}) - \sin(\omega t - \mathbf{k}_m \cdot \mathbf{r})]}{1 + \beta I / I_{\text{SAT}}} \quad (9)$$

where ϵ_0 is the permittivity; $k = |\mathbf{k}_m|$ the wave vector and $\alpha_0 \equiv (\omega / \hbar) N |\mu_{13}|^2 T$ the line-center ($\delta = 0$) small signal field attenuation coefficient.

Using eq. 7b we can get similarly the polarization associated with the subsystem 2, 4 and write:

$$P' = - \frac{\epsilon_0 \alpha'_0}{k (1 + \delta'^2)} \frac{I / I_{\text{SAT}}}{1 + \beta I / I_{\text{SAT}}} \frac{\sum_m \mathbf{A}_m [\delta' \cos(\omega t - \mathbf{k}_m \cdot \mathbf{r}) - \sin(\omega t - \mathbf{k}_m \cdot \mathbf{r})]}{1 + I / I'_{\text{SAT}}} \quad (10)$$

where $\alpha'_0 \equiv (\omega / \hbar) N |\mu_{24}|^2 T'$, $\delta' = (\omega - \omega_{42}) T'$ and

$$I'_{\text{SAT}} = \hbar^2 (1 + \delta'^2) / (|\mu_{24}|^2 T' \tau_{24})$$

The total polarization P_t of the whole system is then

$$P_t = \frac{\epsilon_0 \alpha_0}{k (1 + \delta^2)} \left\{ \sum_m \mathbf{A}_m [\delta (1 + f(I)) \cos(\omega t - \mathbf{k}_m \cdot \mathbf{r}) - (1 + g(I)) \sin(\omega t - \mathbf{k}_m \cdot \mathbf{r})] \right\} (1 + \beta I / I_{\text{SAT}})^{-1} \quad (11)$$

where

$$g(I) = (\alpha'_0 / \alpha_0) (1 + \delta^2) (1 + \delta'^2)^{-1} I / I_{\text{SAT}} (1 + I / I'_{\text{SAT}})^{-1} \quad (12)$$

$$f(I) = (\delta' / \delta) g(I) \quad (13)$$

From the following relation

$$\mathbf{P}_t = \epsilon_0 \sum_m \mathbf{A}_m [\chi' \cos(\omega t - \mathbf{k}_m \cdot \mathbf{r}) - \chi'' \sin(\omega t - \mathbf{k}_m \cdot \mathbf{r})] \quad (14)$$

where $\chi = \chi' + i\chi''$ is the susceptibility, we get using eq. (11)

$$\chi = - \frac{\alpha_0}{k(1 + \delta^2)} \frac{\delta [1 + f(I)] + i[1 + g(I)]}{1 + \beta I / I_{SAT}} \quad (15)$$

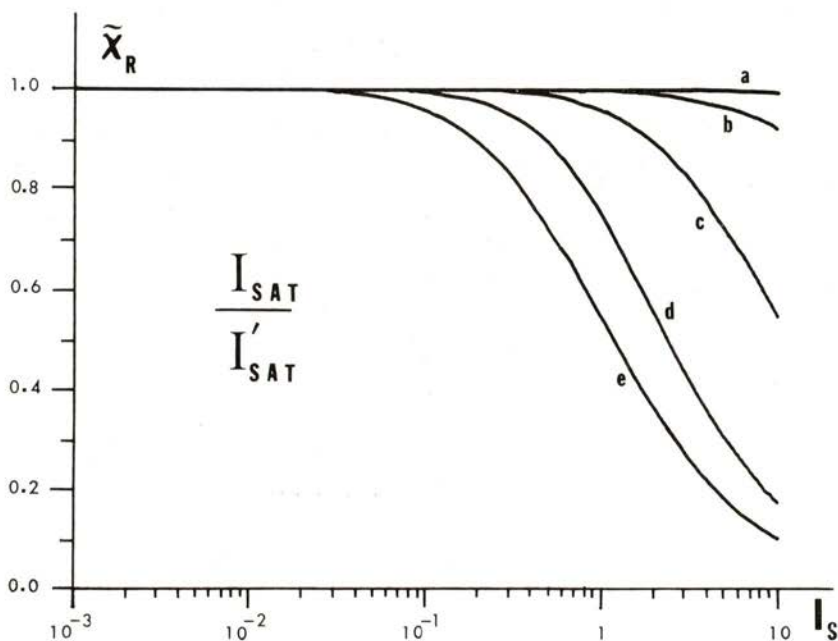


Fig. 7 — Plot of $\chi_R(I_s)$ for different values of the parameter I_{SAT}/I'_{SAT} : Curves a, b, c, d, e correspond to $I_{SAT}/I'_{SAT} = 10^{-3}, 10^{-2}, 10^{-1}, 1, 10$; we have taken $\beta = \alpha'_0/\alpha_0 = \delta' = \delta = 1$.

In Figs. 7 and 8 we show plots of the susceptibility given by the above equation, with different quantities as parameters and where

$$\tilde{\chi} = \tilde{\chi}_R + \tilde{\chi}_I = -\chi k(1 + \delta^2) / \alpha_0 \quad (16)$$

and

$$I_S = I / I_{SAT} \quad (17)$$

In the approximation of neglecting level 4, $f(I)$, $g(I) \ll 1$ and with $\beta = 1$ the complex susceptibility is, as shown in ref. [17],

$$\chi = -(\alpha_0/k)(1 + \delta^2)^{-1} \frac{\delta + i}{1 + I/I_{SAT}} \quad (18)$$

The non-linear nature of χ and consequently of $\mathbf{P} = \epsilon_0 \chi \mathbf{E}$ complicates the solution of the wave equation, describing the light wave propagation inside the medium:

$$\nabla^2 \mathbf{E} - \mu \epsilon_0 \partial^2 \mathbf{E} / \partial t^2 = \mu \partial^2 \mathbf{P} / \partial t^2 \quad (19)$$

where $\mathbf{E}(\mathbf{r}, t)$ is a superposition of plane waves. A similar equation also describes the propagation of each component \mathbf{E}_j coupled to the others by the polarization \mathbf{P} . In FWM, those components refer to the pumps, probe and FWM signal. For \mathbf{E}_j we can write:

$$\nabla^2 \mathbf{E}_j - \mu \epsilon_0 \partial^2 \mathbf{E}_j / \partial t^2 = \mu \partial^2 \mathbf{P} / \partial t^2 |_j, \quad (20)$$

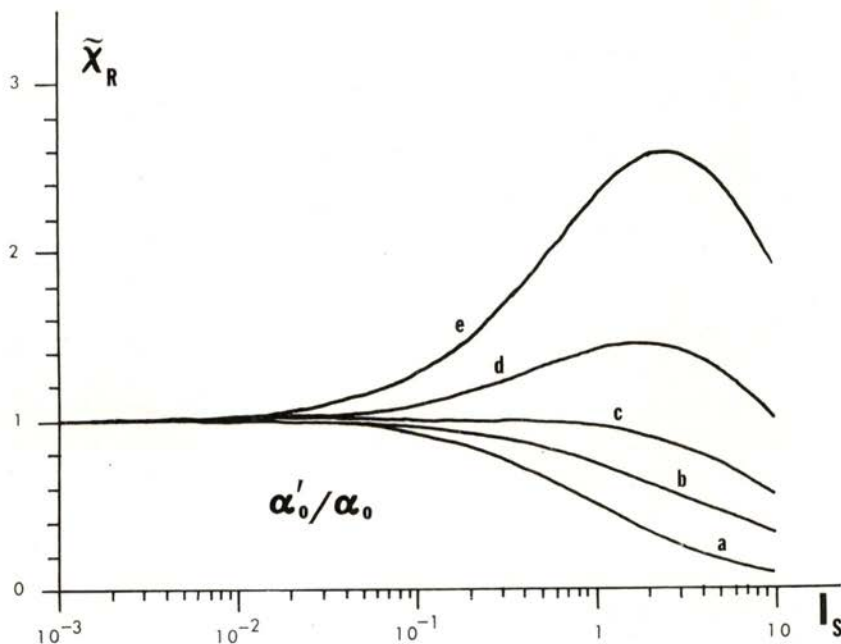


Fig. 8 — Plot of $\tilde{\chi}_R(I_s)$ for different values of the parameter α'_0/α_0 : Curves a, b, c, d, e correspond to $\alpha'_0/\alpha_0 = 0, 0.25, 1, 2, 4$; $\beta = \delta' = \delta = 1$; $I_{SAT}/I'_{SAT} = 0.1$.

where the last term represents the component which matches the phase of the first member of the equation.

We consider A_j a slowly varying function of η_j only, where η_j is the direction of propagation of beam j . Using the adiabatic or Born approximation we can get from (20) a system of coupled differential equations for each amplitude A_j . For $j = 4$ we write:

$$\partial A_4 / \partial z = (\tilde{\alpha} / 2) (A_4 - A_1 A_3^* A_2 / I_{SAT}) \quad (21)$$

where $\tilde{\alpha} = \alpha_0 (1 - i\delta) / (1 + \delta^2)$.

To write eq. 21 we have considered $\phi = 0$ and only the beams 1 and 3 interfering to form an hologram which is read by beam 2.

In general, no analytical solutions are possible for those coupled differential equations. However if $A_{3,4} < A_{1,2}$ such solution is possible either when $I < I_{SAT}$ or $I \geq I_{SAT}$. The solution for the first condition is simpler to get and turns out to be a particular case of that of second one [12].

The expression for the intensity of the phase conjugate signal $I_4(0)$ is [12]:

$$I_4(0) = 2(1 + \delta^2) R T^6 I_1(0)^2 I_3(0) e^{-2\tilde{\alpha}'L} (1 - e^{-\tilde{\alpha}'L})^2 / I_{SAT}^2 \quad (22)$$

where,

$$I_{SAT} = h \omega / (Q \sigma \tau_{21}) = 6.6 \times 10^{21} / (\lambda \sigma) \quad (23)$$

$$\sigma = \tilde{\alpha}' / N_0, \quad \tilde{\alpha}' = \alpha_0 / (1 + \delta^2) \quad (24)$$

R e T are the reflectance and transmittance of the crystal and $Q = 1$.

So far we have considered the non-linear medium as isotropic. However, the ruby crystal is uniaxial and it seems that an anisotropic theory should be needed. The geometry of interaction (propagation direction of the beams, field polarization and c-axis orientation) conditions the validity of application of those theories.

Figs. 9 and 10 show two possible orientations of the crystal, corresponding to propagation of ordinary waves only. However when the crystal is rotated around \hat{n} by an angle θ , ordinary and extraordinary waves propagate in the crystal and the developed isotropic theory is no longer valid. We can apply it however separately to each of the waves, treating them as inde-

pendent of each other. As it will be shown, the relative weights of ordinary and extraordinary waves in the measured FWM signal are dependent on the angle of rotation and the characteristic

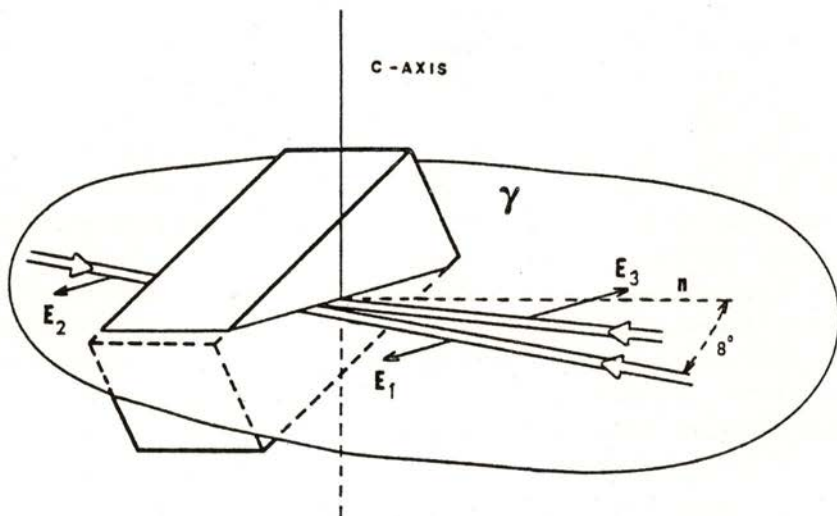


Fig. 9 — Isotropic configuration, with the transversally oriented crystal; the c-axis is normal to plane γ containing the direction of propagation of beams 1, 2 and 3; n is the normal to $5 \times 11 \text{ mm}^2$ surface of the crystal.

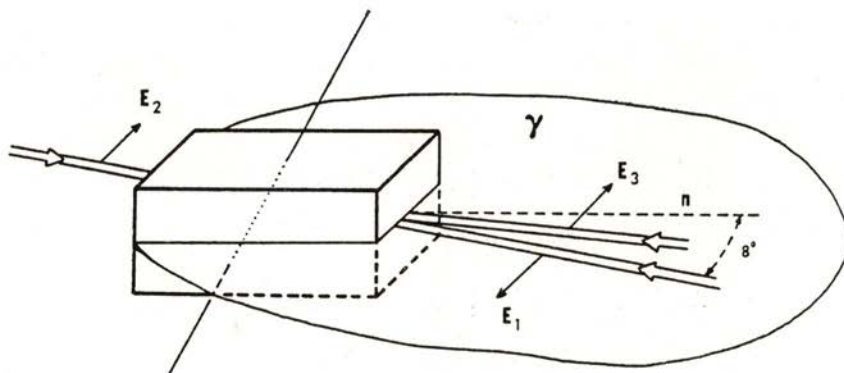


Fig. 10 — Another possible configuration showing the beams 1 and 3 incident on surface $5 \times 5 \text{ mm}^2$. This is the most efficient configuration, because of the largest interaction length.

parameters associated with those waves. In the holographic interpretation of FWM it means that we have two distinct holograms: one called ordinary and the other extraordinary, which do not interact with each other.

With the two configurations shown in Figs. 9 and 10 we can check experimentally the validity of this theory. At the same time we will show different physical behaviour for those configurations. Geometrically the essential difference between transversal and longitudinal orientation of the crystal is that, during crystal rotation, the c-axis remains approximately normal to the propagation direction of the beams in the first case and makes a 60° angle in the second one.

The quantities appearing in eq. 22 that are different for ordinary and extraordinary waves are $\tilde{\alpha}'$ and I_{SAT} . For light propagating in ordinary and extraordinary modes a net absorption coefficient can be defined for transversal and longitudinal configurations, as function of rotation angle θ :

$$\tilde{\alpha}'_T = \tilde{\alpha}'_o \cos^2 \theta + \tilde{\alpha}'_e \sin^2 \theta \quad (25)$$

$$\tilde{\alpha}'_L = \tilde{\alpha}'_o (\cos^2 \theta + \cos^2 \beta \sin^2 \theta) + \tilde{\alpha}'_e \sin^2 \beta \sin^2 \theta \quad (26)$$

where β , the angle between \hat{n} and c-axis, is 60°.

Fig. 11 shows the theoretical curves given by eqs. 25 and 26 and the experimental data for $\tilde{\alpha}'_T$ and $\tilde{\alpha}'_L$ as functions of θ .

In analogy with eq. 21, the differential equations for A_4^o and A_4^e (the indices o and e stand for "ordinary" and "extraordinary") can be written as:

$$\partial A_4^o / \partial z = 1/2 \tilde{\alpha}_o \{ A_4^o - [(A_1^o \cdot A_3^{o*}) / I_{SAT}^o + (A_1^e \cdot A_3^{e*}) / I_{SAT}^e] A_2^o \} \quad (27a)$$

$$\partial A_4^e / \partial z = 1/2 \tilde{\alpha}_e \{ A_4^e - [(A_1^o \cdot A_3^{o*}) / I_{SAT}^o + (A_1^e \cdot A_3^{e*}) / I_{SAT}^e] A_2^e \} \quad (27b)$$

The physical interpretation of the above equation is that the ordinary (extraordinary) component of beam 2 is scattered by both ordinary and extraordinary gratings. However this may not

be the case if the Bragg condition is not satisfied for both waves. In this case, \mathbf{A}_2^o (\mathbf{A}_2^e) will be scattered only by the ordinary (extraordinary) grating. The equations 27a, b will become:

$$\partial \mathbf{A}_4^o / \partial z = 1/2 \tilde{\alpha}_o [\mathbf{A}_4^o - (\mathbf{A}_1^o \cdot \mathbf{A}_3^{o*}) \mathbf{A}_2^o / I_{SAT}^o] \quad (28a)$$

$$\partial \mathbf{A}_4^e / \partial z = 1/2 \tilde{\alpha}_e [\mathbf{A}_4^e - (\mathbf{A}_1^e \cdot \mathbf{A}_3^{e*}) \mathbf{A}_2^e / I_{SAT}^e] \quad (28b)$$

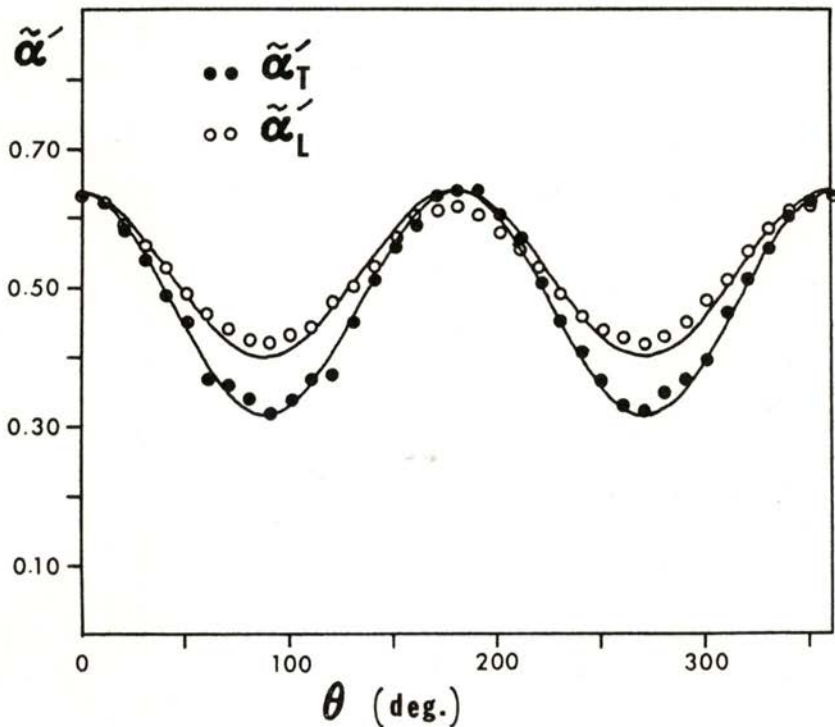


Fig. 11 — Experimental data points and theoretical curves for $\tilde{\alpha}'_T$ and $\tilde{\alpha}'_L$ as a function of rotation angle θ , for transversal (Fig. 9) and longitudinal (Fig. 10) orientation of the crystal.

The expressions for the intensity $I_4 = I_4^o + I_4^e$ (with $I = \mathbf{A} \cdot \mathbf{A}^* / 2$) which correspond to those physical situations are [18]

$$I_4(0) = 1/8 (|B_o|^2 \cos^2 \theta + |B_e|^2 \sin^2 \theta) / (C_o \cos^2 \theta + C_e \sin^2 \theta)^2 \quad (29)$$

from eq. 27, and

$$I_4^B(0) = 1/8 (|B_o|^2 C_o^2 \cos^6 \theta + |B_e|^2 C_e^2 \sin^6 \theta) \quad (30)$$

from eq. 28, where

$$B_o \equiv B (\tilde{\alpha}_o / 2) \exp (- \tilde{\alpha}_o L) , \quad (31a)$$

$$B_e \equiv B (\tilde{\alpha}_e / 2) \exp (- \tilde{\alpha}_e L) , \quad (31b)$$

$$B \equiv A_1^2(0) A_3^*(0) \sqrt{R} , \quad (32)$$

$$C_o \equiv [\exp (- \tilde{\alpha}'_o L) - 1] / \tilde{\alpha}'_o I_{SAT}^o , \quad (33a)$$

$$C_e \equiv [\exp (- \tilde{\alpha}'_e L) - 1] / \tilde{\alpha}'_e I_{SAT}^e ; \quad (33b)$$

4 - EXPERIMENTAL RESULTS

The experiments have been performed in order to check the validity of eq. 22 for the isotropic configuration and eqs. 29 and 30 for the anisotropic one. Fig. 12 shows the set-up used to measure the DFWM signal.

A - Isotropic configuration

The orientation of the crystal used for testing eq. 22, is shown in Fig. 9. In this way, only ordinary waves propagate in the crystal. Since the quantity we measured was the power of the 4 different beams, the expression given by eq. 22 had to be modified. The beams have been considered to have Gaussian shapes and their radii have been measured or calculated. Written in terms of measured powers \tilde{P}_4 and \tilde{P}_1 eq. 22 becomes:

$$\tilde{P}_4 = C (1 + \delta^2) \tilde{P}_1^3 (\mu W, \text{cm}) \quad (34)$$

where C depends on the beams' diameters and all the parameters affecting I_4 in eq. 22.

Fig. 13 shows the theoretical curves for different wavelengths of the Ar laser, when $\delta = 0$. In Fig. 14 we show experimental

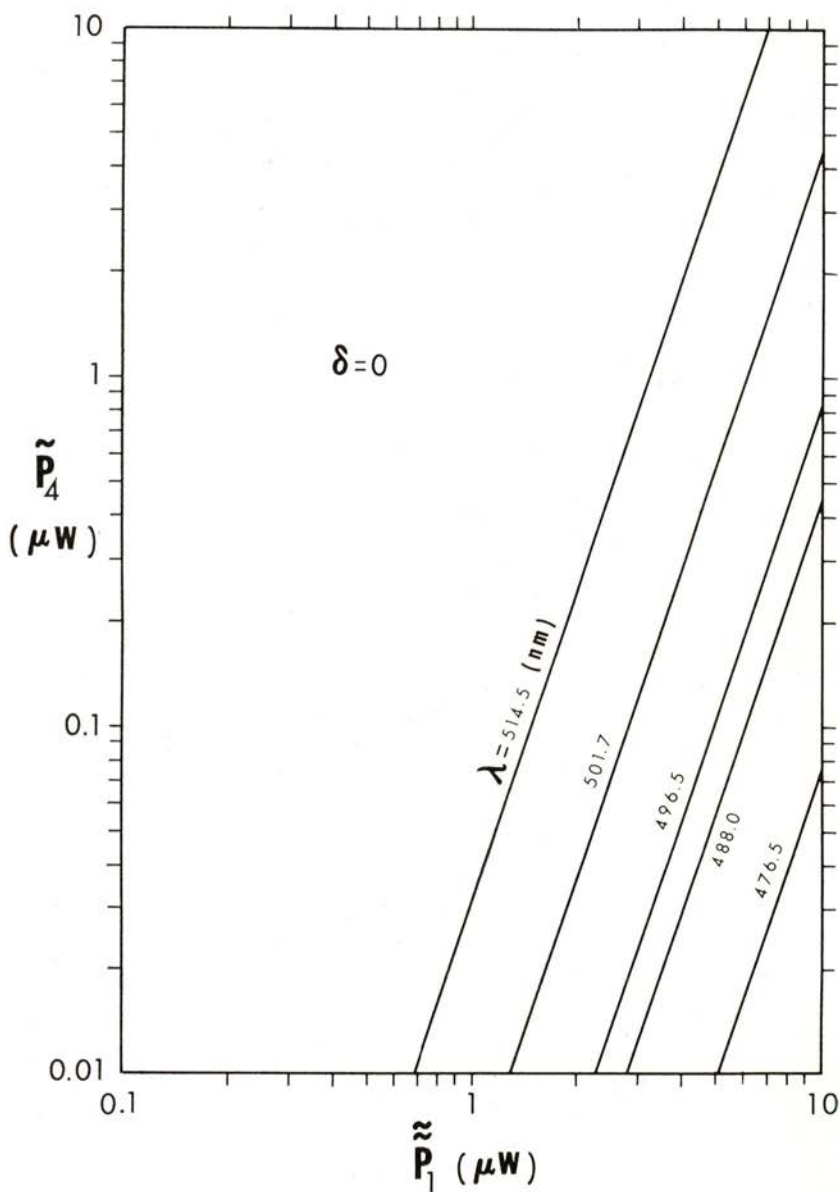


Fig. 13 — Theoretical curves for $\delta = 0$ predicted by eq. 34. Each line corresponds to a different wavelength λ of the Ar laser.

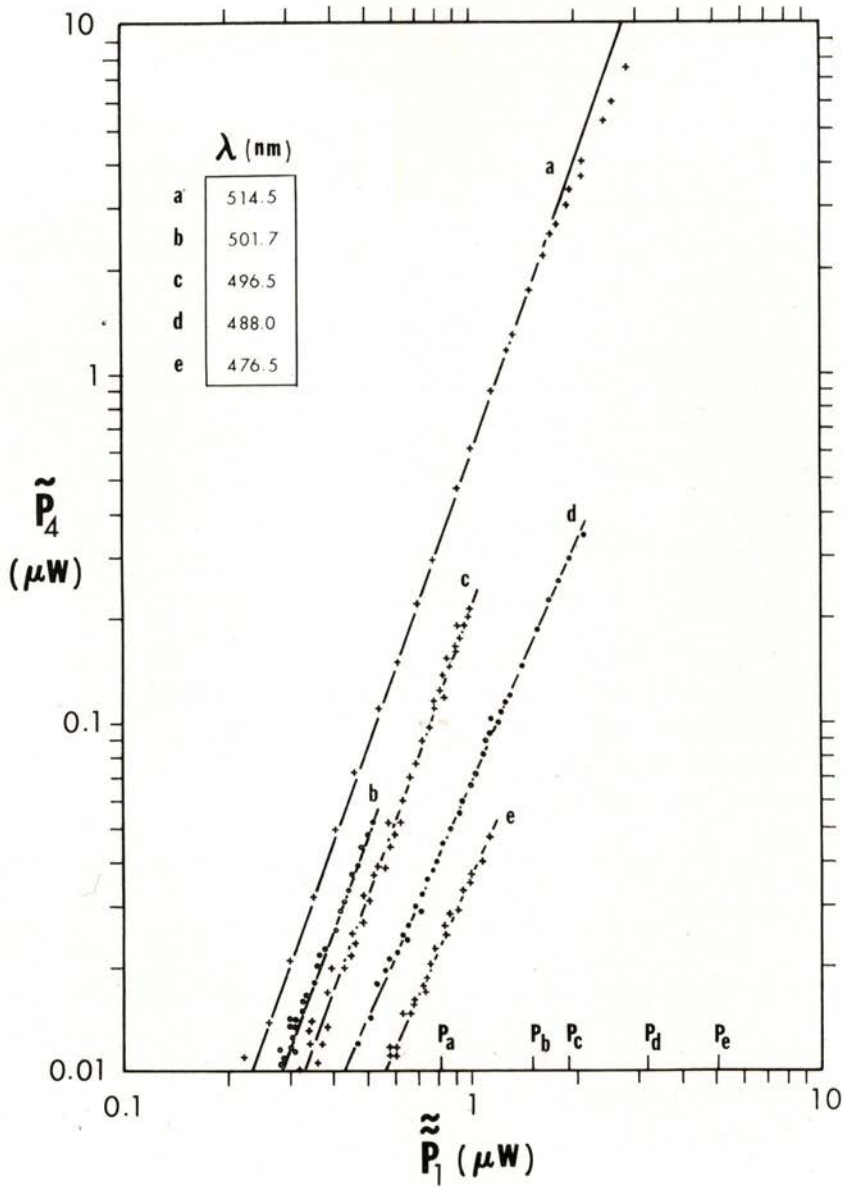


Fig. 14 — Experimental points for \tilde{P}_4 as function of \tilde{P}_1 , with wavelength λ as a parameter. The lines are the best linear fitting.

data for the same wavelengths and where $\tilde{P}_x = 10^{-2} \tilde{P}_{SAT}$ for $\lambda = \lambda_x$ and $x = a, b, c, d, e$.

When we try to fit the experimental data with the theoretical curves we get the following conclusions [12]:

- a) δ (unknown independently) depends on the wavelength.
- b) Curves *a, b, c* show a slope close to 2; however *d* and *e* deviate from that slope.
- c) For large \tilde{P}_1 , curve *a* starts deviating from linear behaviour.

The behaviour of curves *d* and *e* has been attributed to the increase of beams' diameters with the electric current in the laser.

The non-linearity of curve *a* for large enough valumes of \tilde{P}_1 is due to the proximity of \tilde{P}_{SAT} .

B — Anisotropic configuration

i) Transversal orientation for the crystal

With the crystal orientation shown in Fig. 9, we rotate the crystal by an angle θ around the direction of propagation k_1 .

The theoretical expressions for P_4 derived from eqs. 29 and 30, after substituting for the values of the parameters in eqs. 31, 32 and 33, are respectively:

$$P_4(0) \propto (\cos^2 \theta + 0.34 \sin^2 \theta) (\cos^2 \theta + 0.54 \sin^2 \theta)^2 \quad (35)$$

$$P_4^B(0) \propto \cos^6 \theta + 0.1 \sin^6 \theta \quad (36)$$

The theoretical curves and the experimental data are shown in Fig. 15. The full-line corresponds to eq. 35 and the dashed-line to eq. 36. The best fitting is obtained with eq. 35, showing that the ordinary and extraordinary components of reading beam 2 are diffracted by both ordinary and extraordinary gratings.

ii) Longitudinal orientation for the crystal

The crystal has been positioned as in Fig. 10 and rotated around \hat{k} , as in i). The experimental expressions for P_4 derived

from eqs. 29 and 30 are, after substituting for the numerical values of the parameters, respectively:

$$P_4(0) \propto (\cos^2 \theta + 0.7 \sin^2 \theta) (\cos^2 \theta + 0.74 \sin^2 \theta)^2 \quad (37)$$

$$P_4^B(0) \propto \cos^6 \theta + 0.4 \sin^6 \theta \quad (38)$$

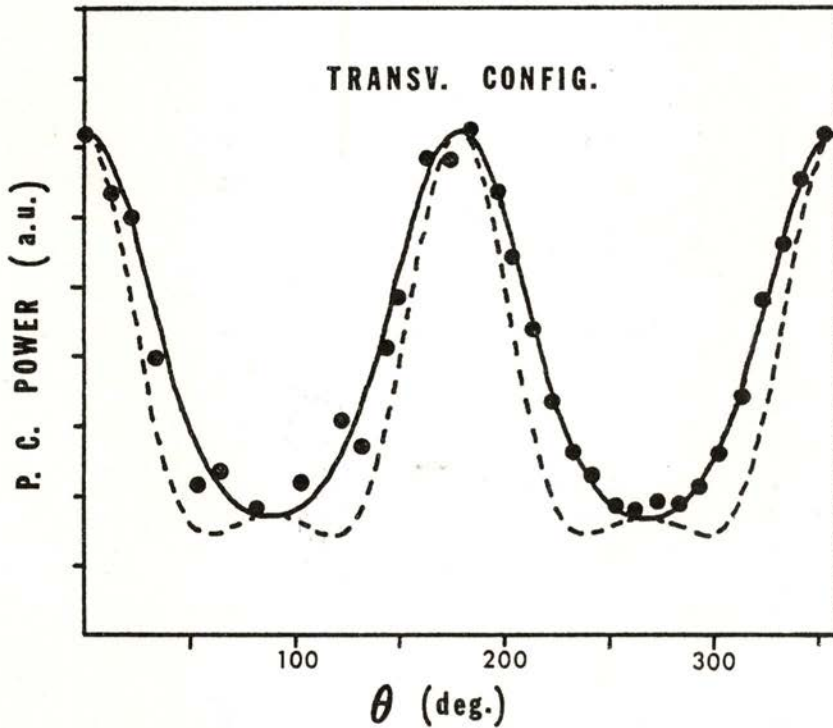


Fig. 15—Experimental data points and theoretical curves for FWM signal (P. C. Power) as a function of the rotation angle in the transversal configuration. Full line corresponds to eq. 35 and dashed line to eq. 36. The power units are arbitrary (a. u.).

The theoretical curves and the experimental data are shown in Fig. 16. The best fitting (full-line) corresponds to eq. 38.

From the above results we can conclude that, in the longitudinal orientation, the ordinary (extraordinary) beam 2 does

not satisfy the Bragg condition for the extraordinary (ordinary) grating.

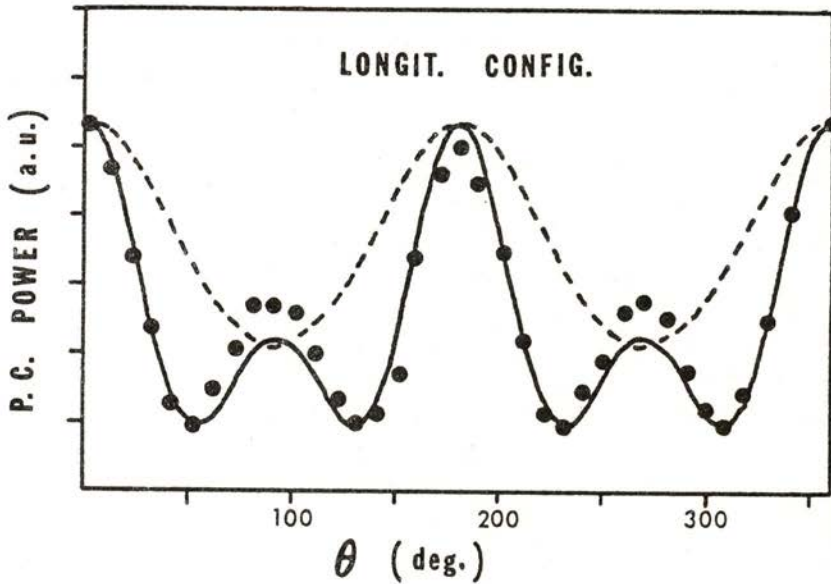


Fig. 16 — Experimental data points and theoretical curves for FWM signal (P. C. Power) as a function of the rotation angle in the longitudinal configuration. Full line corresponds to eq. 38 and dashed line to eq. 37. The power units are arbitrary (a. u.).

5 — THERMAL DFWM

Because of the nonradiative decay from level 3 to level 2 (see fig. 3), a thermal grating is also formed in the crystal. Since the index of refraction changes with temperature ($dn/dT = 12.6 \times 10^{-6} \text{ K}^{-1}$) a phase grating due to temperature will result.

The expression for the FWM signal intensity $I_4^{\text{th}}(0)$ due to this effect is [12]:

$$I_4^{\text{th}}(0) = R T^6 (4\pi \cdot 10^{-13}/\lambda)^2 e^{-3\tilde{\alpha}'L} (1 - e^{-\alpha'L})^2 I_1^2(0) I_3(0), \quad (39)$$

which when compared with $I_4(0)$ given by eq. 22 turns out to be $\sim 10^{-10}$ smaller! This is the consequence of the high thermal

conductivity ($\lambda = 0.42 \text{ W cm}^{-1} \text{ K}^{-1}$) of ruby causing the wash out of the thermal grating very effectively and rapidly (decay time $\sim 10^{-8} \text{ s}$).

6 — SELF-FOCUSING

Self-focusing gives rise to a deformation of a beam profile with non-uniform intensity and results from non-uniform changes in the optical properties of the medium, caused by the beam itself. Wavefront deformations of the beams used in FWM may, therefore, exist due to self-focusing. Such deformations can somehow affect the measured phase conjugate signal, as suggested in ref. 19.

Two mechanisms can be responsible for self-focusing: non-uniform distribution of temperature and of energy level excitation.

Theoretically, for the typical powers used in our experiment, the phase delay $\Delta\phi$ between the center and the edge of the Gaussian beam are $\Delta\phi_1 = 0.2 \text{ rad}$ and $\Delta\phi_2 = 0.15 \text{ rad}$ respectively [12]. The radii of curvature have been calculated to be $R_1 = 23 \text{ m}$ and $R_2 = 66 \text{ m}$. Those values are small when compared with the intrinsic laser beam divergence.

Experimentally we have used both Moiré and double exposure holographic interferometry techniques [12]. We did not observe any curvature effect with $\Delta\phi > \pi$, the maximum sensitivity of the used techniques.

Such results lead us to conclude that for the power levels we used in our c.w. DFWM experiments the self-focusing effects can be neglected.

7 — PHASE CONJUGATION — AN APPLICATION OF FWM

Phase conjugation refers to any process in which a wave

$$\mathbf{E}_4(\mathbf{r}, t) = \text{Re} [\mathbf{A}_4(\mathbf{r}) e^{i\omega t}] \quad (40)$$

is generated from an incident wave

$$\mathbf{E}_3(\mathbf{r}, t) = \text{Re} [\mathbf{A}_3(\mathbf{r}) e^{i\omega t}] \quad (41)$$

and the relation between their amplitudes is

$$\mathbf{A}_4(\mathbf{r}) = R \mathbf{A}_3^*(\mathbf{r}), \quad (42)$$

where R is a constant; Re stands for "real part of" and $*$ for "complex conjugate".

For simplicity we consider the case of 'plane waves'. If we write

$$A_3 = \psi(\mathbf{r}) e^{-ikz} \quad (43)$$

and because of the identity

$$\begin{aligned} E_4(\mathbf{r}, t) &= \text{Re} [R \psi^*(\mathbf{r}) e^{ikz} e^{i\omega t}] = \text{Re} [R \psi^*(\mathbf{r}) e^{ikz} e^{i\omega t}]^* \\ &= \text{Re} [R \psi(\mathbf{r}) e^{-ikz} e^{-i\omega t}] = \text{Re} [R A_3(\mathbf{r}) e^{-i\omega t}], \end{aligned} \quad (44)$$

we can say that E_4 is the time reversal of $R E_3$, i. e. E_4 is equal to $R E_3$ after t becomes $-t$. Phase conjugation and time reversal are therefore often used with the same meaning. The above discussion is also valid for non-plane waves if the superposition principle applies.

The solution of eq. 21 shows that A_4 is proportional to A_3^* i. e. the FWM signal 4 is the phase conjugate of probe 3.

To show the phase conjugate imaging properties of FWM we introduce a resolution chart in our set-up as shown in Fig. 17. The orientation of the crystal is that shown in Fig. 10, which corresponds to maximum efficiency because of the larger interaction length L .

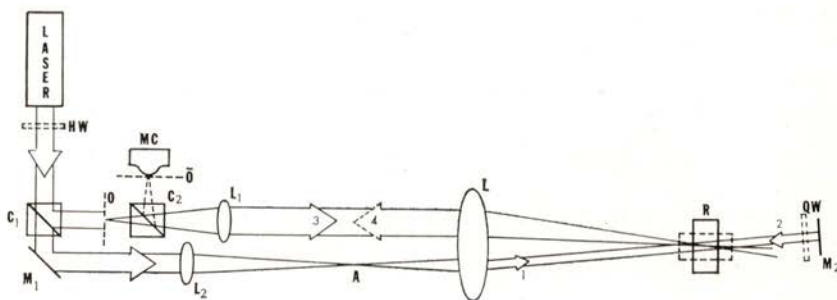


Fig. 17 — Schematic of the experimental set-up (the same as in Fig. 12) for the phase conjugate reconstruction of a microscopic object. 0 and $\bar{0}$ are the object and the phase conjugate object planes. MC is a microscope with a photographic camera.

The input and the phase conjugate image are shown in Fig. 18a, b. A speckle averaging technique has been used [20], to improve the image quality. It consists in moving the crystal

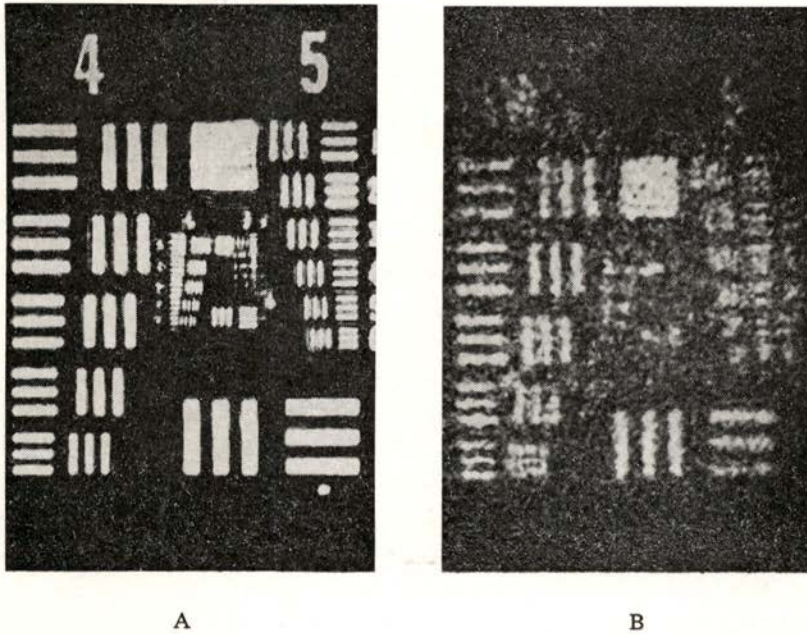


Fig. 18 — (a) Input object in plane 0 (b) phase conjugate reconstructed object after speckle averaging: multiple (15) exposure $15 \times 1/125$ sec. The spatial frequency of 5-1 group is ~ 30 line pairs/mm.

continuously during exposure or by steps with multiple exposure. This can be also accomplished by phase modulation of one of the beams which causes in addition, by averaging the grating contrast, a more uniform intensity of the image.

The author would like to thank Prof. S. P. Almeida for fruitful discussions and Instituto Nacional de Investigação Científica for financial support. Part of this work has been done in Virginia Polytechnic Institute and State University.

REFERENCES

- [1] C. V. HEER and N. C. GRIFFEN, *Opt. Lett.*, **4**, 239 (1978). A. MARUANI, *IEEE J. Quantum Electron.*, **QE-16**, 558 (1980). A. L. SMIRL, T. F. BOGGESS and F. A. HOPF, *Opt. Comm.*, **34**, 463 (1980).
- [2] N. BLOEMBERGEN, *Nonlinear Optics* (W. A. Benjamin, Inc., New York, 1965).
- [3] P. D. MAKER and R. W. TERHUNE, *Phys. Rev.*, **A137**, 801 (1965).
- [4] A. YARIV, *IEEE J. Quantum Electron.*, **QE-14**, 650 (1978); *Opt. Comm.*, **25**, 23 (1978).
- [5] B. I. STEPANOV, E. V. IVAKIN, A. S. RUBANOV, *Sov. Phys. Dokl.*, **16**, 44 (1971).
- [6] D. G. STEEL and J. F. LAM, *Phys. Rev. Lett.*, **43**, 1588 (1979).
- [7] A. E. SIEGMAN, *An Introduction to Lasers and Masers* (McGraw-Hill Book Company, New York, 1971).
- [8] T. KUSHIDA, *J. Phys. Soc. Japan*, **21**, 1331 (1966).
- [9] M. J. WEBER, *Methods of Experimental Physics*, vol. 15-A: Quantum Electronics, ed. C. L. Tang (Academic Press, New York, 1979).
- [10] T. H. MAINMAN, R. H. HOSKINS, I. J. D'HAENES, C. K. ASAWA and V. EVTUHOV, *Phys. Rev.*, **123**, 1151 (1961).
- [11] W. M. FAIRBANK, Jr., G. K. KLAUMINZER and A. L. SCHAWLOW, *Phys. Rev.*, **B11**, 60 (1975).
- [12] L. M. BERNARDO, Ph. D. THESIS, Virginia Polytechnic Institute and State University, Blacksburg, Virginia 24061 (1983).
- [13] Th. HANSCH and P. TOSCHEK, *Z Physik*, **236**, 213 (1970).
- [14] U. FANO, *Rev. Mod. Phys.*, **29**, 74 (1957).
- [15] G. ORRIOLS, *Il Nuovo Cimento*, **53B**, 1 (1979).
- [16] E. I. SHTYRKOV, *Opt. Spectrosc.*, **45**, 339 (1979).
- [17] R. L. ABRAMS, R. C. LIND, *Opt. Lett.*, **2**, 94 (1978).
- [18] L. M. BERNARDO, S. P. ALMEIDA, *Opt. Comm.*, **48**, 389 (1984).
- [19] P. F. LIAO, D. M. BLOOM, *Opt. Lett.*, **3**, 4 (1978).
- [20] L. M. BERNARDO, S. P. ALMEIDA, *Appl. Opt.*, **22**, 3926 (1983).